DArT in ArDM

Technical Design Report

March 28, 2019

The DarkSide-20k and

the Global Argon Dark Matter Collaboration

C. E. Aalseth,[1] S. Abdelhakim,[2] F. Acerbi,[3, 4] P. Agnes,[5] I. F. M. Albuquerque,[6] T. Alexander,[1]
A. Alici,[7, 8] A. K. Alton,[9] P. Amaudruz,[10] F. Ameli,[11] P. Antonioli,[8] S. Arcelli,[7, 8] R. Ardito,[12, 13]
I. J. Arnquist,[1] P. Arpaia,[14, 15] D. M. Asner,[16] A. Asunskis,[17] M. Ave,[6] H. O. Back,[1] A. Barrado Olmedo,[18]
G. Batignani,[19, 20] M. G. Bisogni,[19, 20] V. Bocci,[11] A. Bondar,[21, 22] G. Bonfini,[23] W. Bonivento,[24]
B. Bottino,[25, 26] M. G. Boulay,[27] R. Bunker,[1] S. Bussino,[28, 29] A. Buzulutskov,[21, 22] M. Cadeddu,[30, 24]
M. Cadoni,[30, 24] A. Caminata,[26] N. Canci,[5, 23] A. Candela,[23] C. Cantini,[31] M. Caravati,[24] M. Cariello,[26]
M. Carpinelli,[32, 33] A. Castellani,[12, 13] P. Castello,[34, 24] S. Catalanotti,[35, 15] V. Cataudella,[35, 15]
P. Cavalcante,[36, 23] S. Cavuoti,[35, 15] S. Cebrian,[37] B. Celano,[15] R. Cereseto,[26] W. Cheng,[38, 39]
A. Chepurnov,[40] C. Cicalò,[24] L. Cifarelli,[7, 8] M. Citterio,[13] A. G. Cocco,[15] M. Colocci,[7, 8] L. Consiglio,[41]
F. Cossio,[38, 39] G. Covone,[35, 15] P. Crivelli,[31] I. D'Antone,[8] M. D'Incecco,[23] D. D'Urso,[32, 33]
M. D. Da Rocha Rolo,[38] M. Daniel,[18] S. Davini,[26] A. De Candia,[35, 15] S. De Cecco,[11, 42] M. De Deo,[23]
A. De Falco,[24, 30] G. De Filippis,[35, 15] D. De Gruttola,[43] G. De Guido,[44, 13] G. De Rosa,[35, 15]
G. Dellacasa,[38] P. Demontis,[32, 33, 45] S. DePaquale,[43] A. V. Derbin,[46] A. Devoto,[30, 24] F. Di Eusanio,[47, 23]
G. Di Pietro,[23, 13] P. Di Stefano,[48] C. Dionisi,[11, 42] F. Dordei,[24] M. Downing,[49] F. Edalatfar,[10] A. Empl,[5]
M. Fernandez Diaz,[18] A. Ferri,[3, 4] C. Filip,[50] G. Fiorillo,[35, 15] K. Fomenko,[51] A. Franceschi,[52] D. Franco,[53]
G. E. Froudakis,[54] F. Gabriele,[23] A. Gabrieli,[32, 33] C. Galbiati,[47, 41] P. Garcia Abia,[18] D. Gascón Fora,[55]
A. Gendotti,[31] C. Ghiano,[23] A. Ghisi,[12, 13] S. Giagu,[11, 42] P. Giampa,[10] R. A. Giampaolo,[38] C. Giganti,[56]
M. A. Giorgi,[20, 19] G. K. Giovanetti,[47] M. L. Gligan,[50] A. Gola,[3, 4] O. Gorchakov,[51] M. Grab,[57]
R. Graciani Diaz,[55] F. Granato,[58] M. Grassi,[19] J. W. Grate,[1] G. Y. Grigoriev,[59] M. Gromov,[40]
M. Guan,[60] M. B. B. Guerra,[17] M. Guerzoni,[8] M. Gulino,[61, 33] R. K. Haaland,[62] B. R. Hackett,[63]
A. Hallin,[64] B. Harrop,[47] E. W. Hoppe,[1] S. Horikawa,[41, 23] B. Hosseini,[24] F. Hubaut,[65] P. Humble,[1]
E. V. Hungerford,[5] An. Ianni,[47, 23] V. Ippolito,[11] C. Jillings,[66, 67] S. Jimenez Cabre,[18] K. Keeter,[17]
C. L. Kendziora,[68] S. Kim,[58] I. Kochanek,[23] K. Kondo,[41] G. Kopp,[47] D. Korablev,[51] G. Korga,[5, 23]
A. Kubankin,[69] R. Kugathasan,[38, 39] M. Kuss,[19] M. Kuzniak,[27] M. La Commara,[70, 15] M. Lai,[30, 24]
S. Langrock,[66, 67] M. Lebois,[2] B. Lehnert,[64] X. Li,[47] Q. Liqiang,[2] M. Lissia,[24] G. U. Lodi,[44, 13]
G. Longo,[35, 15] R. Lussana,[71, 13] L. Luzzi,[72, 13] A. A. Machado,[73] I. N. Machulin,[59, 74] A. Mandarano,[41, 23]
L. Mapelli,[47] M. Marcante,[75, 4, 3] M. Marcante,[75, 4, 3] S. M. Mari,[28, 29] M. Mariani,[72, 13] J. Maricic,[63]
M. Marinelli,[25, 26] D. Marras,[24] A. D. Martinez Rojas,[38, 39] C. J. Martoff,[58] M. Mascia,[76, 24] A. Masoni,[24]
A. Mazzi,[3, 4] A. B. McDonald,[48] A. Messina,[11, 42] P. D. Meyers,[47] T. Miletic,[63] R. Milincic,[63]
A. Moggi,[19] S. Moioli,[44, 13] J. Monroe,[77] M. Morrocchi,[19] T. Mroz,[57] W. Mu,[31] V. N. Muratova,[46]
S. Murphy,[31] C. Muscas,[34, 24] P. Musico,[26] R. Nania,[8] T. Napolitano,[52] A. Navrer Agasson,[56]
M. Nessi,[78] I. Nikulin,[69] A. O. Nozdrina,[59, 74] N. N. Nurakhov,[59] A. Oleinik,[69] V. Oleynikov,[21, 22]
M. Orsini,[23] F. Ortica,[79, 80] L. Pagani,[81] M. Pallavicini,[25, 26] S. Palmas,[76, 24] L. Pandola,[33] E. Pantic,[81]
E. Paoloni,[19, 20] G. Paternoster,[3, 4] V. Pavletcov,[40] F. Pazzona,[32, 33] S. Peeters,[82] P. A. Pegoraro,[34, 24]
K. Pelczar,[23] L. A. Pellegrini,[44, 13] N. Pelliccia,[79, 80] F. Perotti,[12, 13] V. Pesudo,[18] E. Picciau,[30, 24]
C. Piemonte,[3, 4] F. Pietropaolo,[78] A. Pocar,[49] T. Pollman,[83] D. Portaluppi,[71, 13] S. S. Poudel,[5]
P. Pralavorio,[65] D. Price,[84] D. A. Pugachev,[59] B. Radics,[31] F. Raffaelli,[19] F. Ragusa,[85, 13] M. Razeti,[24]
A. Razeto,[23] V. Regazzoni,[75, 4, 3] C. Regenfus,[31] A. L. Renshaw,[5] S. Rescia,[16] M. Rescigno,[11]
F. Retiere,[10] Q. Riffard,[53] A. Rivetti,[38] A. Romani,[79, 80] L. Romero,[18] N. Rossi,[11, 23] A. Rubbia,[31]
D. Sablone,[58, 23] P. Sala,[78] P. Salatino,[86, 15] O. Samoylov,[51] E. Sànchez Garcìa,[18] S. Sanfilippo,[29, 28]
M. Sant,[32, 33] D. Santone,[77] R. Santorelli,[18] C. Savarese,[47] E. Scapparone,[8] B. Schlitzer,[81] G. Scioli,[7, 8]
E. Segreto,[73] A. Seifert,[1] D. A. Semenov,[46] A. Shchagin,[69] E. Shemyakina,[21, 22] A. Sheshukov,[51]
S. Siddhanta,[24] M. Simeone,[86, 15] P. N. Singh,[5] P. Skensved,[48] M. D. Skorokhvatov,[59, 74] O. Smirnov,[51]
G. Sobrero,[26] A. Sokolov,[21, 22] A. Sotnikov,[51] R. Stainforth,[27] S. Stracka,[19] G. B. Suffritti,[32, 33, 45]
S. Sulis,[34, 24] Y. Suvorov,[35, 15, 59] A.M. Szelc,[84] R. Tartaglia,[23] G. Testera,[26] T. Thorpe,[41, 23]
A. Tonazzo,[53] A. Tosi,[71, 13] E. V. Unzhakov,[46] G. Usai,[24, 30] A. Vacca,[76, 24] E. Vázquez-Jáuregui,[87]
M. Verducci,[11, 42] T. Viant,[31] S. Viel,[27] F. Villa,[71, 13] A. Vishneva,[51] B. Vogelaar,[36] M. Wada,[24]
J. Wahl,[1] J. J. Walding,[77] H. Wang,[88] Y. Wang,[88] S. Westerdale,[27] R. J. Wheadon,[38] R. Williams,[1]
J. Wilson,[2] Marcin Wojcik,[57] Mariusz Wojcik,[89] S. Wu,[31] X. Xiao,[88] C. Yang,[60] Z. Ye,[5] and G. Zuzel[57]

[1]*Pacific Northwest National Laboratory, Richland, WA 99352, USA*
[2]*Institut de Physique Nuclèaire dOrsay, 91406, Orsay, France*
[3]*Fondazione Bruno Kessler, Povo 38123, Italy*

ii

[4] *Trento Institute for Fundamental Physics and Applications, Povo 38123, Italy*
[5] *Department of Physics, University of Houston, Houston, TX 77204, USA*
[6] *Instituto de Física, Universidade de São Paulo, São Paulo 05508-090, Brazil*
[7] *Physics Department, Università degli Studi di Bologna, Bologna 40126, Italy*
[8] *INFN Bologna, Bologna 40126, Italy*
[9] *Physics Department, Augustana University, Sioux Falls, SD 57197, USA*
[10] *TRIUMF, 4004 Wesbrook Mall, Vancouver, BC V6T 2A3, Canada*
[11] *INFN Sezione di Roma, Roma 00185, Italy*
[12] *Civil and Environmental Engineering Department, Politecnico di Milano, Milano 20133, Italy*
[13] *INFN Milano, Milano 20133, Italy*
[14] *Department of Electrical Engineering and Information Technology,*
Università degli Studi "Federico II" di Napoli, Napoli 80125, Italy
[15] *INFN Napoli, Napoli 80126, Italy*
[16] *Brookhaven National Laboratory, Upton, NY 11973, USA*
[17] *School of Natural Sciences, Black Hills State University, Spearfish, SD 57799, USA*
[18] *CIEMAT, Centro de Investigaciones Energéticas, Medioambientales y Tecnológicas, Madrid 28040, Spain*
[19] *INFN Pisa, Pisa 56127, Italy*
[20] *Physics Department, Università degli Studi di Pisa, Pisa 56127, Italy*
[21] *Budker Institute of Nuclear Physics, Novosibirsk 630090, Russia*
[22] *Novosibirsk State University, Novosibirsk 630090, Russia*
[23] *INFN Laboratori Nazionali del Gran Sasso, Assergi (AQ) 67100, Italy*
[24] *INFN Cagliari, Cagliari 09042, Italy*
[25] *Physics Department, Università degli Studi di Genova, Genova 16146, Italy*
[26] *INFN Genova, Genova 16146, Italy*
[27] *Department of Physics, Carleton University, Ottawa, ON K1S 5B6, Canada*
[28] *INFN Roma Tre, Roma 00146, Italy*
[29] *Mathematics and Physics Department, Università degli Studi Roma Tre, Roma 00146, Italy*
[30] *Physics Department, Università degli Studi di Cagliari, Cagliari 09042, Italy*
[31] *Institute for Particle Physics, ETH Zürich, Zürich 8093, Switzerland*
[32] *Chemistry and Pharmacy Department, Università degli Studi di Sassari, Sassari 07100, Italy*
[33] *INFN Laboratori Nazionali del Sud, Catania 95123, Italy*
[34] *Department of Electrical and Electronic Engineering Engineering, Università degli Studi, Cagliari 09042, Italy*
[35] *Physics Department, Università degli Studi "Federico II" di Napoli, Napoli 80126, Italy*
[36] *Virginia Tech, Blacksburg, VA 24061, USA*
[37] *Laboratorio de Física Nuclear y Astropartículas, Universidad de Zaragoza, Zaragoza 50009, Spain*
[38] *INFN Torino, Torino 10125, Italy*
[39] *Department of Electronics and Communications, Politecnico di Torino, Torino 10129, Italy*
[40] *Skobeltsyn Institute of Nuclear Physics, Lomonosov Moscow State University, Moscow 119234, Russia*
[41] *Gran Sasso Science Institute, L'Aquila 67100, Italy*
[42] *Physics Department, Sapienza Università di Roma, Roma 00185, Italy*
[43] *INFN Salerno, Salerno 84084, Italy*
[44] *Chemistry, Materials and Chemical Engineering Department "G. Natta", Politecnico di Milano, Milano 20133, Italy*
[45] *Interuniversity Consortium for Science and Technology of Materials, Firenze 50121, Italy*
[46] *Saint Petersburg Nuclear Physics Institute, Gatchina 188350, Russia*
[47] *Physics Department, Princeton University, Princeton, NJ 08544, USA*
[48] *Department of Physics, Engineering Physics and Astronomy, Queen's University, Kingston, ON K7L 3N6, Canada*
[49] *Amherst Center for Fundamental Interactions and Physics*
Department, University of Massachusetts, Amherst, MA 01003, USA
[50] *National Institute for R&D of Isotopic and Molecular Technologies, Cluj-Napoca, 400293, Romania*
[51] *Joint Institute for Nuclear Research, Dubna 141980, Russia*
[52] *INFN Laboratori Nazionali di Frascati, Frascati 00044, Italy*
[53] *APC, Université Paris Diderot, CNRS/IN2P3, CEA/Irfu, Obs de Paris, USPC, Paris 75205, France*
[54] *Department of Chemistry, University of Crete, P.O. Box 2208, 71003 Heraklion, Crete, Greece*
[55] *Universiatat de Barcelona, Barcelona E-08028, Catalonia, Spain*
[56] *LPNHE, CNRS/IN2P3, Sorbonne Université, Université Paris Diderot, Paris 75252, France*
[57] *M. Smoluchowski Institute of Physics, Jagiellonian University, 30-348 Krakow, Poland*
[58] *Physics Department, Temple University, Philadelphia, PA 19122, USA*
[59] *National Research Centre Kurchatov Institute, Moscow 123182, Russia*
[60] *Institute of High Energy Physics, Beijing 100049, China*
[61] *Engineering and Architecture Faculty, Università di Enna Kore, Enna 94100, Italy*
[62] *Department of Physics and Engineering, Fort Lewis College, Durango, CO 81301, USA*

[63] Department of Physics and Astronomy, University of Hawai'i, Honolulu, HI 96822, USA

[64] Department of Physics, University of Alberta, Edmonton, AB T6G 2R3, Canada

[65] Centre de Physique des Particules de Marseille, Aix Marseille Univ, CNRS/IN2P3, CPPM, Marseille, France

[66] Department of Physics and Astronomy, Laurentian University, Sudbury, ON P3E 2C6, Canada

[67] SNOLAB, Lively, ON P3Y 1N2, Canada

[68] Fermi National Accelerator Laboratory, Batavia, IL 60510, USA

[69] Radiation Physics Laboratory, Belgorod National Research University, Belgorod 308007, Russia

[70] Pharmacy Department, Università degli Studi "Federico II" di Napoli, Napoli 80131, Italy

[71] Electronics, Information, and Bioengineering Department, Politecnico di Milano, Milano 20133, Italy

[72] Energy Department, Politecnico di Milano, Milano 20133, Italy

[73] Physics Institute, Universidade Estadual de Campinas, Campinas 13083, Brazil

[74] National Research Nuclear University MEPhI, Moscow 115409, Russia

[75] Physics Department, Università degli Studi di Trento, Povo 38123, Italy

[76] Department of Mechanical, Chemical, and Materials Engineering, Università degli Studi, Cagliari 09042, Italy

[77] Department of Physics, Royal Holloway University of London, Egham TW20 0EX, UK

[78] CERN, European Organization for Nuclear Research 1211 Geneve 23, Switzerland, CERN

[79] Chemistry, Biology and Biotechnology Department, Università degli Studi di Perugia, Perugia 06123, Italy

[80] INFN Perugia, Perugia 06123, Italy

[81] Department of Physics, University of California, Davis, CA 95616, USA

[82] Physics and Astronomy, University of Sussex, Brighton BN1 9QH, UK

[83] Physik Department, Technische Universität München, Munich 80333, Germany

[84] The University of Manchester, Manchester M13 9PL, United Kingdom

[85] Physics Department, Università degli Studi di Milano, Milano 20133, Italy

[86] Chemical, Materials, and Industrial Production Engineering Department,
Università degli Studi "Federico II" di Napoli, Napoli 80126, Italy

[87] Instituto de Física, Universidad Nacional Autónoma de México (UNAM), México 01000, Mexico

[88] Physics and Astronomy Department, University of California, Los Angeles, CA 90095, USA

[89] Institute of Applied Radiation Chemistry, Lodz University of Technology, 93-590 Lodz, Poland

CONTENTS

I. CONTEXT

The DarkSide collaboration published in 2018 two world leading results for WIMP dark matter search for spin-independent interaction: the world best upper limit at low masses, between 1.8 GeV/c^2 and 6 GeV/c^2 [1, 2] and the best upper limit for high masses, above 30 GeV/c^2 [3], for argon targets. One crucial ingredient for achieving these results was the use of argon depleted in the radioactive ^{39}Ar isotope by a factor 1400 compared to atmospheric argon (AAr) that has a radioactivity of about 1 Bq/Kg.

All collaborations pursuing first-generation liquid argon detectors, ArDM, DarkSide, DEAP-3600 and Mini-Clean, recently merged into the Global Argon Dark Matter Collaboration (GADMC), with the purpose of pursuing together the proposed DarkSide-LowMass (1 tonne), DarkSide-20k (20 tonnes) and Argo (300 tonnes) experiments, aiming at investigating WIMP masses above 1 GeV/c^2 with cross sections down to the neutrino floor [4].

DarkSide-20k is an approved project by INFN (Italy) and NSF (USA). A proposal for DarkSide-LowMass will be presented in the Fall 2019.

Two important steps of this research program are Urania, the 250 kg/day underground argon extraction plant to be deployed in Colorado, now in advanced tendering process and scheduled to start operations in 2021, and Aria, the 350 m cryogenic distillation plant in construction in Sardinia, Italy, that will achieve a factor of 10 ^{39}Ar suppression per pass at a rate of 10 kg/day. Aria is expected to enter operations in the second half of 2019.

For DarkSide-20k it is expected that the argon extracted in Colorado will be shipped to Sardinia where it

will undergo chemical purification to be transformed into detector-grade argon at the rate of 1 ton/day, and from there shipped to LNGS.

For DarkSide-Low Mass, which requires only a ton of argon, a distillation step with Aria to suppress further the ^{39}Ar content is foreseen. Aria will enter operations before Urania and its test is a priority for the GADMC.

II.   PROPOSED EXPERIMENT AND GOALS

In this Technical Design Report (TDR), we describe the *DArT in ArDM* experiment at LSC aiming at measuring an ^{39}Ar depletion of order 1000 with 10% precision.

The experiment *DArT in ArDM* is meant to re-using the ArDM infrastructure [5] with a minimal modification, consisting of locating in the middle of the ArDM vessel a radio-pure copper single-phase liquid argon detector of about one litre active volume, named DArT. DArT will be filled with the argon to be tested and be readout by two cryogenic SiPMs of 1 cm^2, that come, together with the readout electronics, from the DarkSide-20k production chain.

The ArDM detector for this experiment should act as an active veto against internal and external radiation. For this purpose we are building a dedicated single phase setup with a new set of low-radioactive photo-multipliers (PMT), while we retain the entire present double phase setup for later use, e.g. for measurements on large quantities of depleted argon [6].

Extensive GEANT4-based simulations of the setup were performed with tuned-on-data MC, inherited from the DarkSide-50 experiment at LNGS.

These simulations show that *DArT in ArDM* will achieve in this configuration a % measurement for ^{39}Ar depletions of order 10 compared to AAr in about a week of running and a 2% measurement for depletions of order 100 (statistical uncertainty only).

This setup will be very useful, if deployed in a timely manner, to characterize the performance of Aria, that is expected to suppress the ^{39}Ar content by a factor of 10 per pass. To achieve this, first goal we need *DArT in ArDM* to be ready by the second half of 2019.

A very important addition to the above described setup will consist of adding 6 ton lead belt of about 1.4 m height, around the ArDM vessel, at mid height position, to suppress the impact of external photons that dominate the background budget. This will allow to measure larger ^{39}Ar depletion, corresponding to those of the argon coming from deep wells underground in Colorado, from the Urania plant.

If the depletion levels are those already measured in the past (i.e. of 1400), it will be possible, according to our simulations, to measure them with a 7% uncertainty in a about a week of running. Upper limits can be set on depletions of order 25200 (statistical uncertainty only), i.e. UAr with one distillation pass in Aria.

The argon from Urania is expected to be available only at the end of 2021. However, it is planned that, after the run of DarkSide-50 at LNGS, presumably at the end of 2019, its argon will be measured in *DArT in ArDM* to cross-check the old measurement and to test the new setup.

This *DArT in ArDM* experiment is expected to become a facility for the LSC for the years to come since it will be needed to measure samples of the extracted argon from Urania over time.

The scientific relevance of depleted argon goes quite beyond its use in DarkSide-LowMass, DarkSide-20k and Argo and is now being considered also by DUNE, COHERENT and LEGEND experiments.

III.   BASIC TECHNIQUE AND PAST ACCOMPLISHMENTS

The amount of ^{39}Ar in the sample will be determined from fits to the spectral shapes as illustrated in Fig. 1 from data from DarkSide-50 (left) and ArDM (right) experiments.
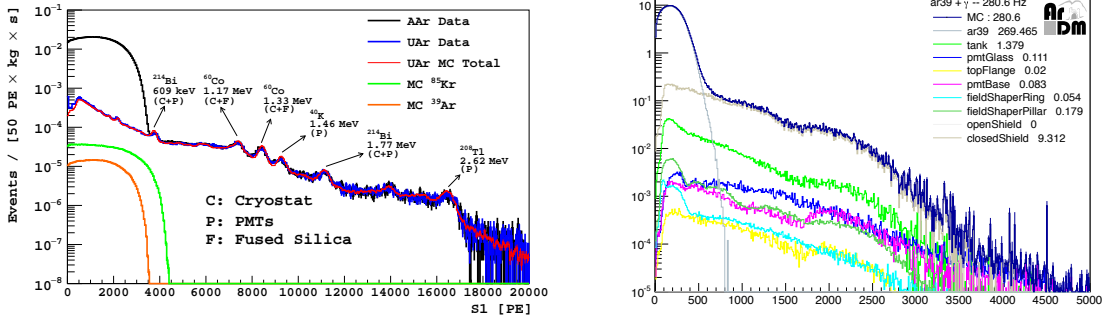
FIG. 1. Examples of background spectra measured with liquid argon detectors for Dark Matter search: DarkSide-50 (left) at LNGS and with ArDM at LSC (right).

DarkSide-50 performed measurements of both atmospheric argon (AAr, black) and underground argon (UAr, red). From fit of the β- spectrum of ^{39}Ar to the background a depletion factor of about 1400 was determined for UAr.

ArDM instead only measured AAr, using a fiducial region of the inner 200 litres, to reduce the external and cryostat background components.

A new measurement has been performed by DEAP-3600, currently being prepared for publication. DArT will benefit from experience of building and operating DEAP-1, which similarly consisted of a small cylindrical wavelength shifter coated acrylic chamber, instrumented with 2 light sensors [7]. DEAP-1 and DEAP-3600 have achieved good light yield and very low surface alpha activity [8–10], which will also be important for DArT

IV. NEW SINGLE PHASE ARDM CONFIGURATION

Fig 2 shows the basic experimental configuration with the DArT chamber in the middle. The dedicated new ArDM single phase configuration is embedded in the 50 cm thick outer polyethylene shielding (not shown) and the stainless steel cryostat with the liquid argon cooling jacket. Similar to the original construction of ArDM the main detector consist of 6 low radioactivity PMT's at the top and 7 at the bottom, surrounded by the reflector foil covered with TPB, entirely attached as a unit to a second top flange which was used for the development of ArDM at CERN. The active liquid argon target amounts to about 0.9 ton in mass.

All this structure is meant to be assembled and tested at CERN together with the DArT chamber in a non-radio-pure acrylic structure. After successful testing it will all be shipped to LSC where also the DArT chamber will be refurbished with the radio-pure acrylic.
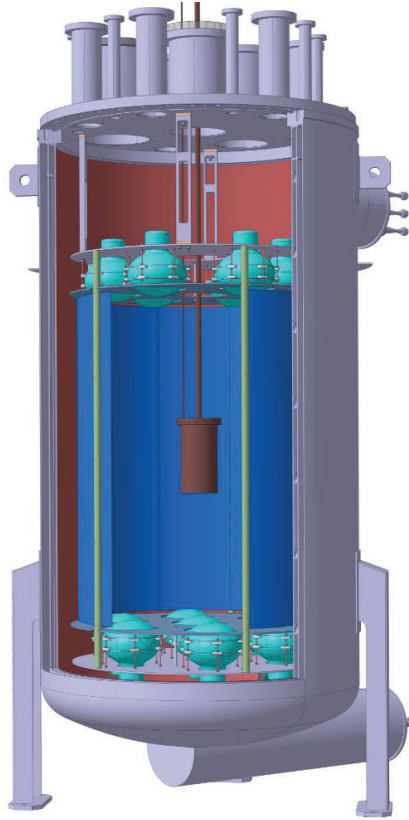
FIG. 2. ArDM cryostat cut view with the new single phase setup and the DART chamber in the middle.

Most of the external background photons that reach DArT come from the lateral side of the detector, due to the smaller distance that external γ's have to travel. For this reason, different lateral external γ shielding have been simulated.

The optimal configuration was obtained with lead belt of 140 cm height and 10 cm width in terms of background reduction and weight (6 tons). The lead belt will be placed at half height of the ArDM detector in the space between the cryostat and the polyethylene shielding, as shown in Fig 3 and Fig 4.
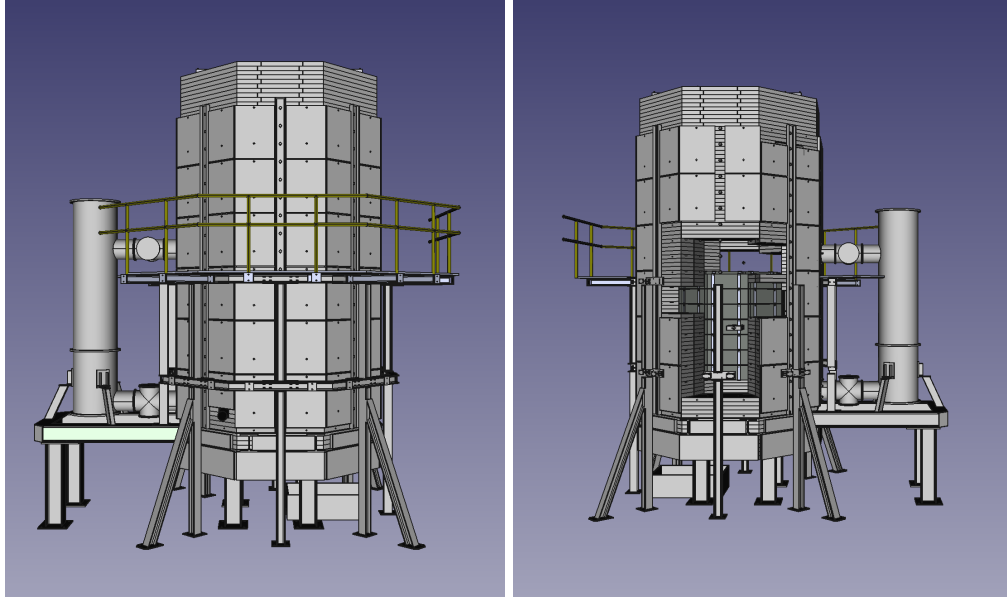
FIG. 3. External view of ArDM (a) and cut view (b) showing the lead belt inside attached to the polyethylene shield (the cryostat was removed in this picture)
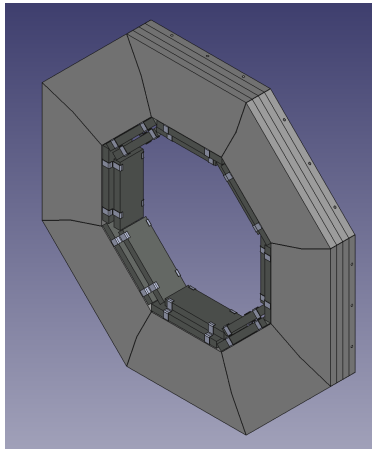

FIG. 4. Horizontal slice of the polyethylene shield with the lead belt (dark) attached to the inner surface

V. DART

A. DArT Mechanics

In order to minimize the possible background given by the intrinsic radioactive contamination of the detector, DArT is built with materials known to be extremely radio-pure like OHFC copper and acrylic (PMMA). In Fig. 5 a technical drawing of the inner part of DArT is shown.
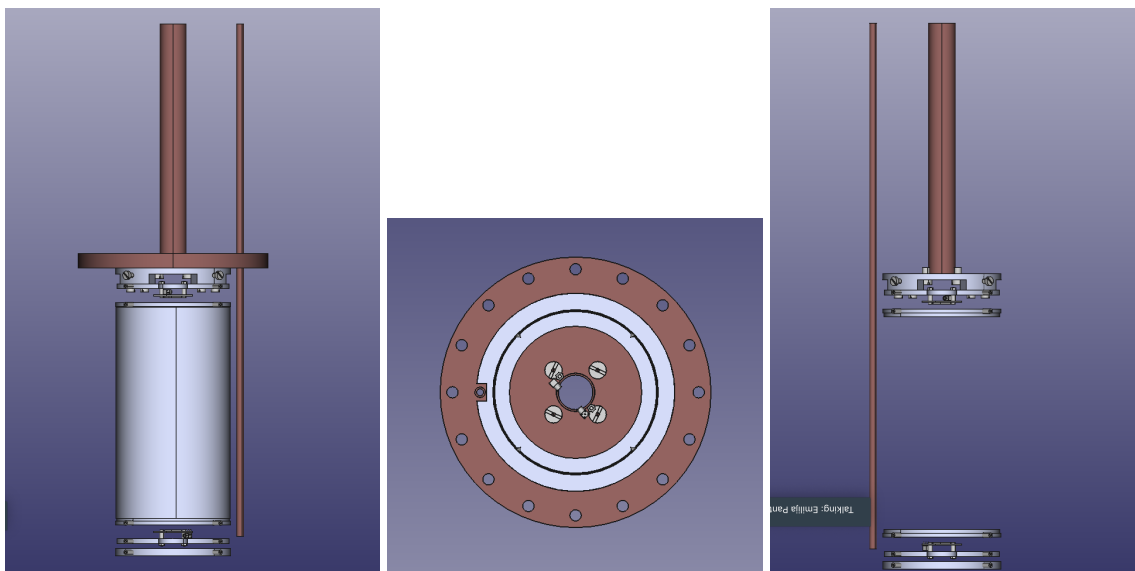
FIG. 5. (a) Side view of the inner structure of DArT, (b) Top view of the inner structure of DArT, (c)Side view of the inner structure of DArT with the innermost part removed

The detector hosting the argon to be tested is made of copper cylinder with 5 mm thick lateral wall and 8 mm thick top/bottom. The machined piece is shown in Fig. 6.
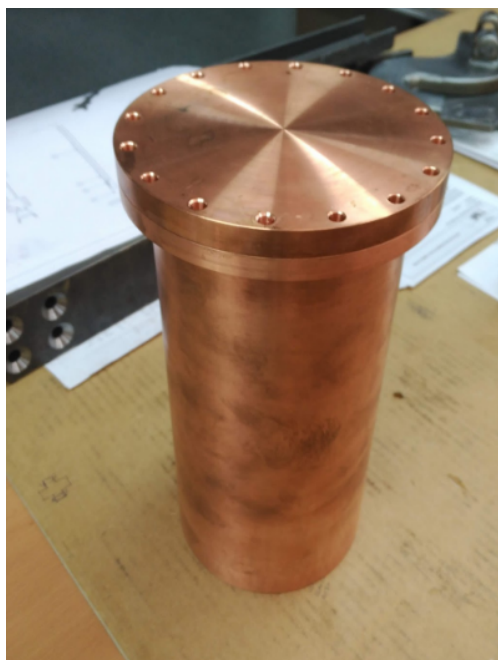

FIG. 6. The DArT copper vessel. The top flange still needs to be machined to accommodate the two copper pipes.

Mechanical simulations showed that such design is able to withstand the maximum pressure foreseen (1 bar) during the evacuation of the vessel inside ArDM. Two copper pipes penetrate inside the vessel, a thinner one going all the way down the vessel allowing the filling of the argon and a larger one stopping at the top flange providing the necessary connections (SiPM HV, signal, level meter etc) through radio-pure cables.

The inner structure is made of an acrylic cylinder, coated with wavelength shifter (TPB) on its inner surface $(200\,\mathrm{g/cm^2})$. The outer surface of the acrylic is enrolled in a Vikuiti reflector foil.

An additional cylinder (annulus) is used as filler of the space outside the reflector foil. A picture of this acrylic piece machined is shown in Fig. 7

FIG. 7. The DArT external acrylic cylinder

The outer acrylic parts will be attached to the top vessel flange, as shown in Fig. 5. The total of the acrylic pieces are 8. They are the following:

- Attachment to the top cover, 1 piece.
- Outer cylinder, 1 piece.
- SiPM support, 2 pieces.
- End cap, 2 pieces.
- Inner cylinder, 1 piece.
- Down facilities support, 1 piece.

Two disk of acrylic of 6 mm thickness with TPB evaporated over the inner surface will be placed between the argon active volume and the two SiPM .

The readout will be performed using one SiPM on the top and one of the bottom from the DarkSide-20k production with a dedicated board attached to another acrylic disk using acrylic screws, as shown in Fig. 8.
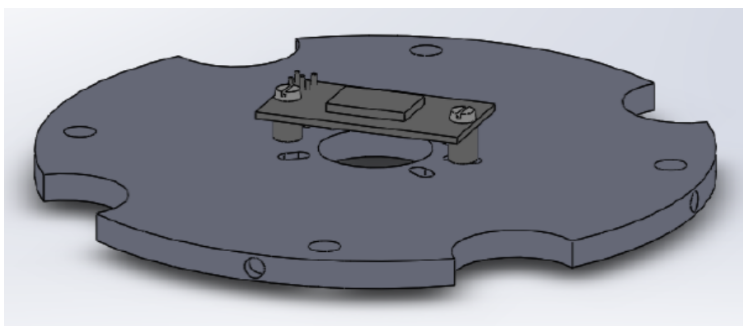

FIG. 8. Top support of DArT acrylic structure housing the FEB.

It is foreseen that for the tests done at CERN the acrylic will not be of the radio-pure type. For the running in LSC it will be very important instead to have the radio-pure version, with proper sanding to

suppress the plate-out of ^{222}Rn daughters.
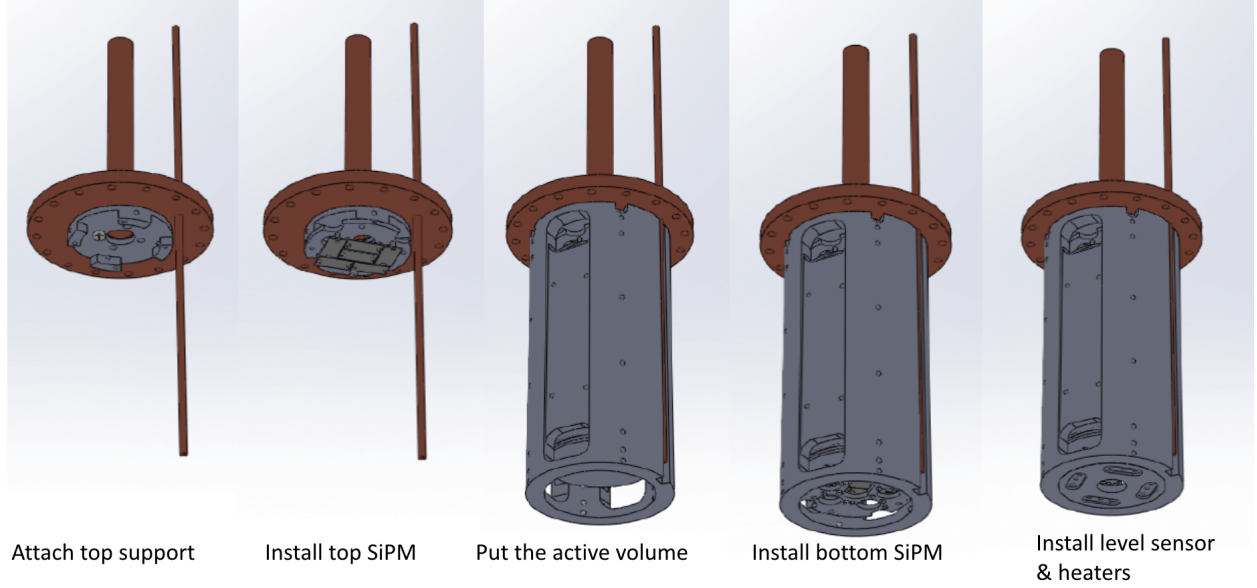Fig. 9 shows the DArT chamber assembly procedure.

| Attach top support | Install top SiPM | Put the active volume | Install bottom SiPM | Install level sensor & heaters |

FIG. 9. DArT chamber assembly procedure

B.   DArT Cryogenics

1.   Integration with ArDM

The DArT chamber is fabricated using ultra pure 99.99% Oxygen Free High Conductivity (OHFC) copper with only 4 ppm of oxygen. It has two 20 cm pipes, see Fig 5, fabricated always with OFHC copper, the smaller one for the argon inlet and the larger one for the argon outlet and for the wiring connecting the instrumentation inside the chamber to the room temperature equipment. A top flange gives access to the inner part of the chamber. All the instrumentation is connected to the top flange, so that removing completely the bottom part of the chamber allows an easy access to our test space and instrumentation.

The two copper pipes are connected, using silver brazing, see Fig. 11 to a structure including the continuation of these 20 cm copper pipes with stainless steel pipes up to the top flange, a CF200 one and the external connections, as shown in Fig. 10.
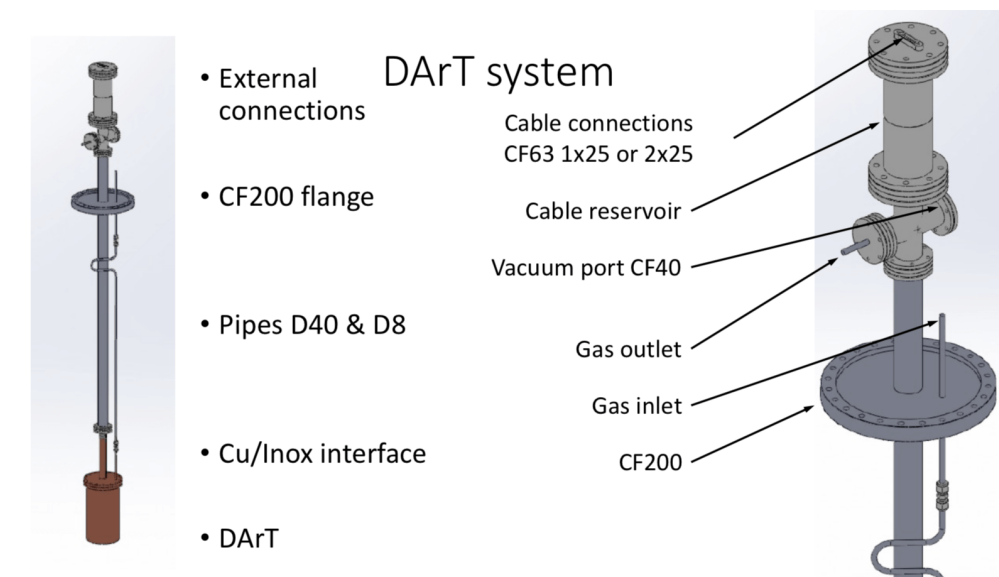
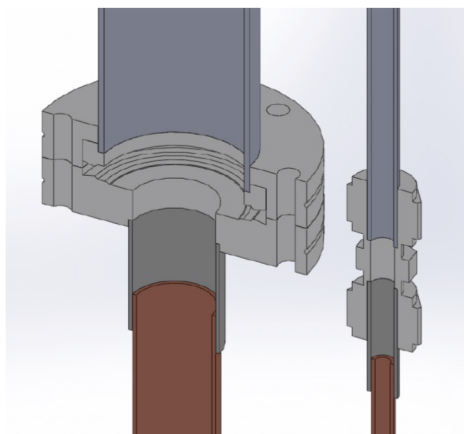FIG. 10. Integration of DArT in the ArDM cryostat

FIG. 11. Integration of DArT in the ArDM cryostat: detail of the connection copper-stainless steel

2. Filling end emptying procedure

a. Initial conditions Less than 1 ppm of oxygen will be left in the evacuated chamber before filling it with argon (larger oxygen traces may quench the scintillation signal produced by the liquid argon), pumping the chamber down to 10^{-3} mbar when still at room temperature.

Refer to Fig. 12 for the following. The chamber may be flushed with atmospheric argon (cylinder B50, AAr) and re-pumped again further decreasing the oxygen content and other possible contaminants. For this purpose we use a pumping system equipped with a turbo pump connected to valve v11. Such a flush and pump procedure may be repeated.
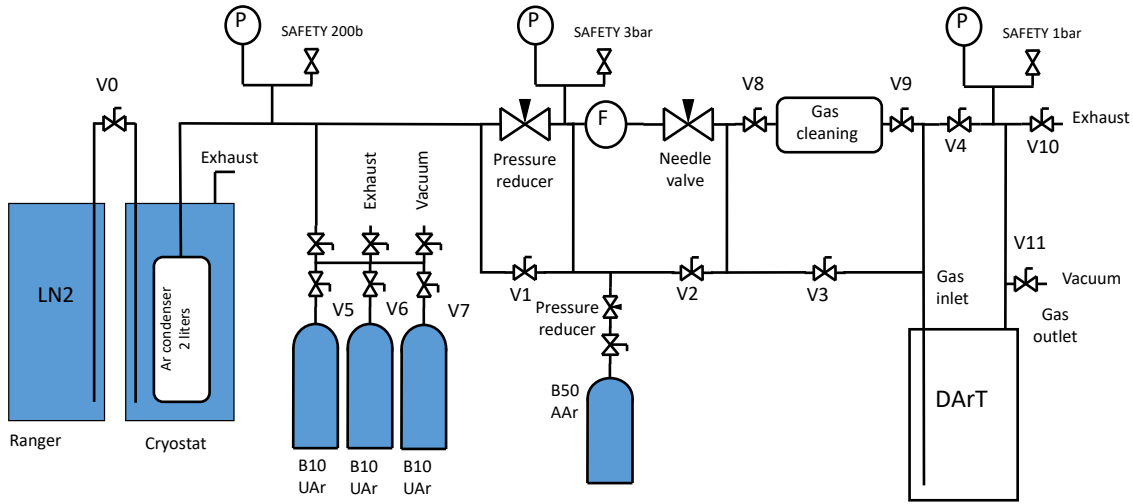
FIG. 12. Schematics of the gas handling system and cryogenics for the operation of the DArT chamber.

An inspection with a helium leak detector at room temperature is performed to assure there are not leaks in the DArT chamber and in the lines at room temperature, where some oxygen might potentially enter. For this purpose the system must be proven leak tight at a level better than 10^{-7} mbar l/s. The turbo pump should be anyway kept on until the system is warm. As an option, being the chamber and pipes volume very small, we may use the leak detector itself, equipped with a turbo pump, to reach the expected level of vacuum. The set of pressure gauges, indicated with P, include a mechanical pressure gauge, a pirani and a cold cathode penning gauge.

After the chamber has been proved leak tight, the underground ArDM cryostat (or the similar "clone" cryostat located at a surface CERN laboratory that will be used during the preliminary tests) is filled with atmospheric liquid argon and the DArT chamber will cool down, the temperature being monitored by the two PT1000 inside the chamber. The SiPM's will cool down slowly enough by conduction through the DART chamber (that is at 87 K) avoiding unnecessary large thermal stresses.

The Turbo pump can now be switched off , v11 closed and the static vacuum pressure in the DArT chamber, read out by the penning pressure gauge is constantly monitored. We expect the pressure to further decrease with the temperature.

b. Filling the DArT chamber with argon The same procedure will be applied twice, in a first step for atmospheric argon to flush the entire system. About 900 litres STP of atmospheric argon gas, stored in the B50 cylinder (e.g. 18 bar, 50 litres) equipped with a pressure regulator, will be used to fill the DArT chamber where it will condense by giving the heat to the ArDM liquid argon target. The gas/liquid density ratio for argon is about 840 referring to gas at STP. After removing the atmospheric argon and pumping the DArT chamber the argon sample to be studied can be filled. The argon will flow through a SAES getter for purification ("Gas cleaning") before reaching the DArT chamber.

The pressure in the DART chamber must be kept at few tens of mbar above the atmospheric pressure, e.g. 0.03 barg to assure that in case of a small leak the argon will not be contaminated. To monitor precisely the pressure, a mechanical pressure gauge working in the range 0-1 barg is placed, at room temperature, between the v4 and v10.

The argon will slowly flow in the DArT chamber and condense therein (without using any pumping system). The speed of the process will be compatible with the ArDM temperature and the slight DArT chamber over-pressure. The final pressure of the argon gas in the lines, after the full condensation of the liquid argon in the chamber, will be approximately 1 bara (0 barg). We estimate that eventually about 840 litres at STP of argon gas will be condensed in the DArT chamber, 50 litres will remain in the cylinder

and less than 10 litres in the room temperature lines. For the underground argon we will use the same procedure, but the source will be the set of cylinders B10 (10 litres each). The fullness of the DArT chamber will be monitored by three PT1000 used as level sensor, exploiting the different self heating of the platinum resistance in gas (3.2mW/K) and in liquid (32mW/K) phase.

    c.   Argon Recovery procedure   To recover the argon in the cylinders (B50 for AAr or B10 for UAr) at room temperature, the procedure is the following. Evaporation is achieved by applying heat power through an electrical resistance, two platinum resistors PT100, driven by a custom circuit. The heater in the DART chamber has to be switched on and due to the poor argon thermal conductivity the heater inside the chamber will assure convection therefore facilitating the argon evaporation. The work required to vaporize the DART liquid argon is 247kJ. With two resistors powered with 3.5W the chamber can be emptied in about 10h. A system test in the laboratory at CIEMAT was performed and worked well. A liquid nitrogen dewar ("cryostat") will be used to cool a 2 litre cylinder ("Ar condenser") where the argon will be condensed and solidified and stored during the recovery procedure. The vapour pressure of solid argon at 77 K is about 270 mbar. A needle valve along the argon path will assure a pressure in the DArT chamber between 700 and 800 mbar, facilitating the evaporation procedure. The different pressure gauges will be used to monitor the pressure inside the "Ar condenser" and inside the DArT chamber. The pressure reducer will assure the desired flow, measured by the flow meter F, of about 90 litres/hour. Once the static pressure inside the DArT chamber is less than 300 mbar we may consider the argon fully recovered. At this stage, the "Ar condenser" may be slowly warmed up to room temperature and eventually the argon gas will be recovered in the proper cylinders (AAr or UAr).

C.   DArT Readout

1.   *Photo-electronics and front-end*

    Two SiPM's from the DarkSide-20k production will be used, one on the top and one on the bottom. The will be wire-bonded to an Arlon $1.5 \times 3\,\mathrm{cm}^2$ board , named *DArTeye*, that will host the front-end on the other side, whose layout and schematics are shown in Figures 13 and 14, respectively. To cope with the needed up to 1 MeV dynamic range linearity, one channel of the front-end designed for DarkSide-20k will be used, with a 10 times larger feedback resistance in the TIA.
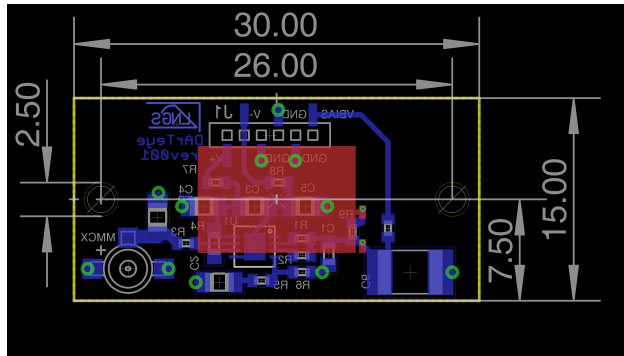

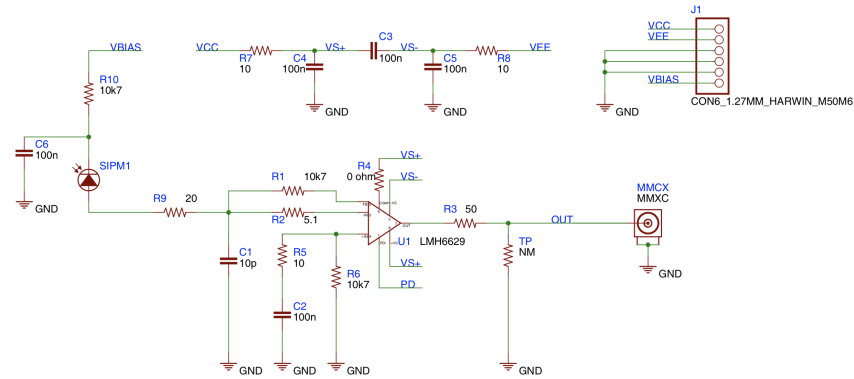FIG. 13. Layout of the DArTeye board .

FIG. 14. Schematics of the DArTeye board

Fig. 15 shows the side and top view of the connection of the DArTeye board to the acrylic support.
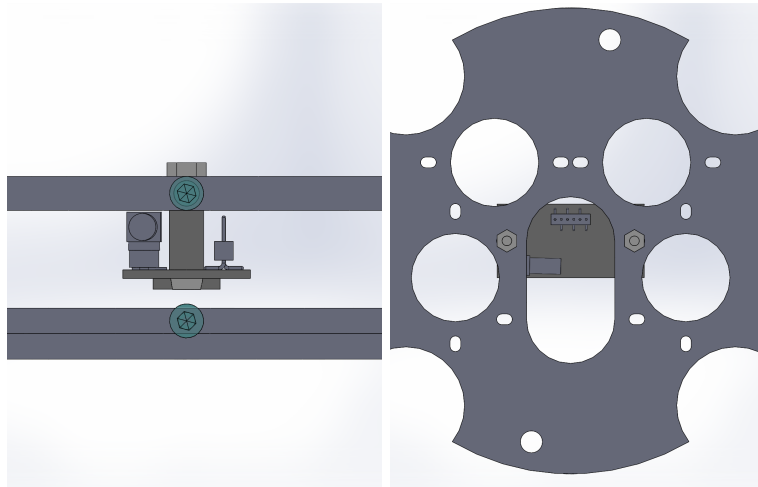

FIG. 15. Side and top view of the connection of the DArTeye board to the acrylic support

2. Simulation of the electronics response

The response of the SiPMs to the scintillation signals was simulated with the DarkSide-20k electronics simulation package. Signals corresponding to α and β particles are shown in Fig. 16.
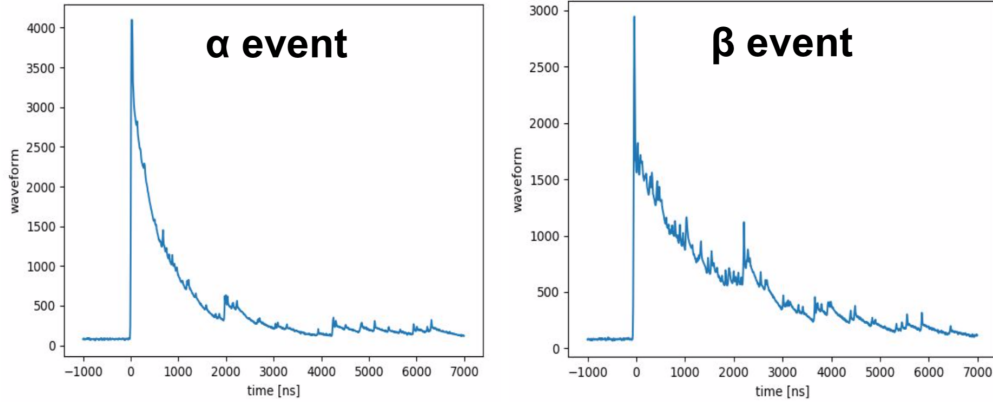
FIG. 16. DArTeye signals corresponding to α and β particles for 500 keV events.

Particle identification with SiPM response is being studied in DarkSide-20k and results for DArT will be provided as soon as possible.

D.   DArT Slow control

1.   Slow control software and hardware

The slow control hardware will be based on National Instrument frames and board and is under design.

2.   Services and wiring

Inside the chamber there are two PT1000 temperature sensors, one placed at the bottom and one at the top, to monitor the temperature and make sure that the chamber is completely topped up with liquid argon at the end of the filling procedure. A heater is also installed providing sufficient power to facilitate the argon evaporation during the recovery procedure. Two SiPM's for the light collection are placed at the bottom and at the top of the chamber. Also an optical fibre reaches the inside of the chamber allowing a calibration of the SiPM's. The fibre will be illuminated by a led that is place just below the connector on the feed-through. Services and wiring are summarized in Tab. I and the electrical characteristics of the services in Tab. II

Service	# of units	# of wires/unit	# of pins on the FT	cable type	connector type on the board
signal SiPM	2	2	4	RG316/RG178	MMCX
LV DArTEye	2	6	12	multi-pole shielded	6 poles 1.27mm pitch
PT1000	3	2	6		
fibre+LED	1	2	2		
heater	2	2	4		
total			28		

TABLE I. Services and wiring for the DArT chamber.

Service	Instrument	$\mathbf{I}_{feed}(\mathbf{mA})$	$\mathbf{V}_{feed}(\mathbf{Volt})$	$\mathbf{P}_{feed}(\mathbf{W})$	type	$\sigma(\mathbf{I})_{mon}(\mathbf{mA})$	$\sigma(\mathbf{V})_{mon}(\mathbf{Volt})$
LV SiPM	Source measure unit		28-35		feed/monitor		0.5
LV TIA	Low noise linear PS		± 2.5		feed/monitor		0.2
PT1000	NI	0.01	0.002		feed/monitor		
LED					feed		
heater(PT100)	power supply	200	17.5	3.5	feed		

TABLE II. Electrical parameters of services for the DArT chamber.

E. DArT Calibration

In principle DArT does not need a ad-hoc energy calibration since the spectrum of ^{39}Ar already provides a calibration. In case a more precise calibration were needed, a possibility would be use the ^{83m}Kr gaseous source, already successfully used with ReD and DarkSide-50. The cryogenic system was conceived with this requirement in mind.

VI. DAQ AND TRIGGER FOR DART IN ARDM

	parameter	# of channels	value (keV)
DArT	channels to be readout	2	1
DArT	Trigger threshold	2	10
DArT	Trigger type		AND
ArDM	channels to be readout	11	20
ArDM	Trigger type		to be defined

TABLE III. DAQ and Trigger requirements. Threshold and signal values for DArT are per SiPM.

The details of the DAQ system need to be defined.
The events will be triggered by DArT or by ArDM. All concurring signals will be recorded for offline study. Parameters are shown in Tab. III.

VII. SIMULATION

A. Geometry

The simulations are based in the GEANT4 Monte Carlo package G4DS that has been developed to simulate the response of DarkSide-50. G4DS embeds a rich set of particle generators, detailed geometry descriptions, properly tuned physical processes, and the full optical propagation of photons produced by scintillation in the liquid argon. It tracks all the generated photons until they reach the active region of the photo-sensors (SiPM's), where they are converted, after surviving a photon detection efficiency cut, into photo-electrons. The geometries of ArDM and DArT detectors have been implemented in detail in the G4DS package. DArT has been simulated as a copper vessel of 5 mm lateral thickness with two pipes on the top flange. The inside part have been simulated as concentric cylinders of underground argon (UAr), a layer of TPB (WLS), acrylic (8 mm), a 3-M foil and another layer of acrylic. Two SiPM-based readout boards are simulated as photo-sensors at the top and bottom sides of the active volume.
The single phase ArDM geometry have been implemented with a liquid argon active volume of 850 kg, and 11 low-radioactivity PMT's (5 top and 6 bottom). The polyethylene shielding, cryostat, internal supports and reflector are included too. A general view of the ArDM geometry with DArT integrated inside is shown in Fig. 17.
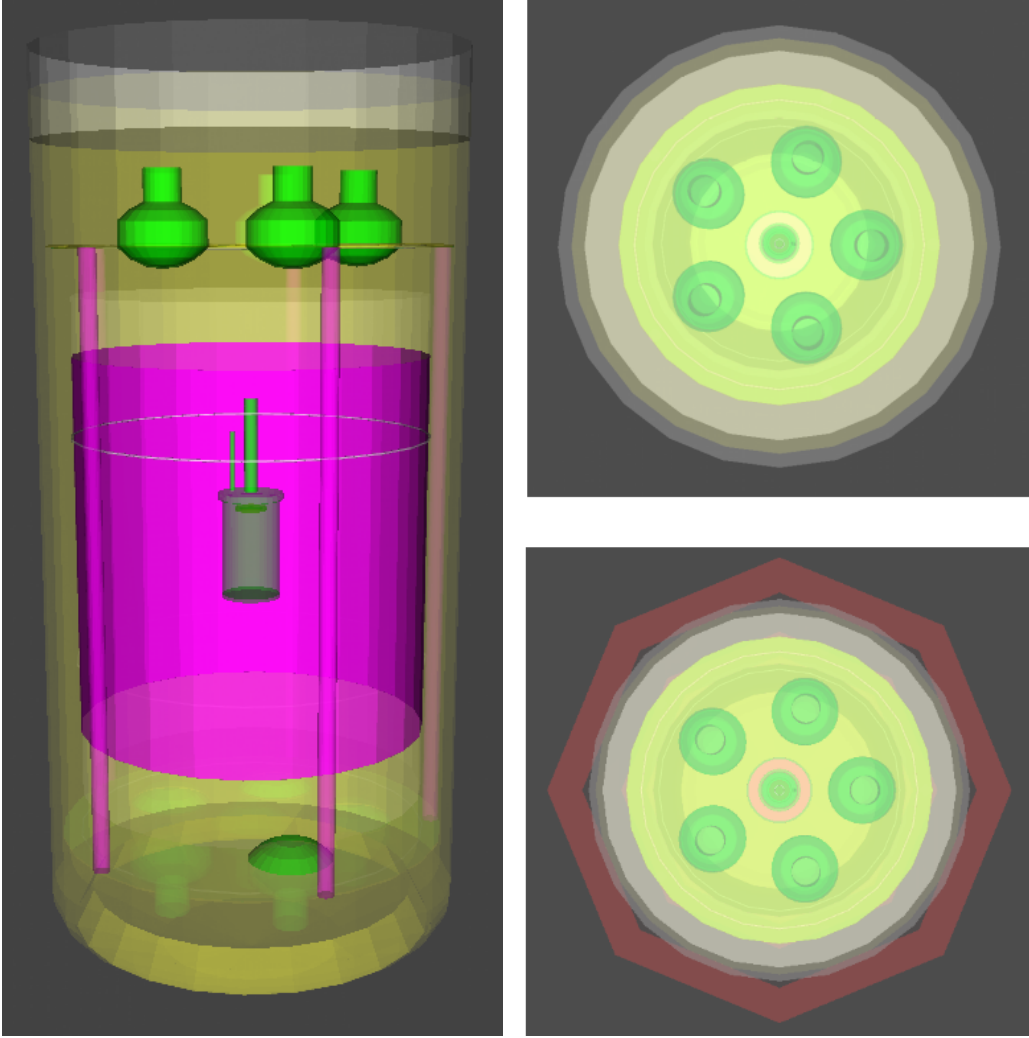
FIG. 17. Lateral and top view of ArDM geometry implemented in G4DS, with DArT integrated. Down-right: Top view with the lead belt integrated (red) around the ArDM cryostat.

The amount of external background events is too large respect to the signal expected (Sec. VII B). Most of these events are coming from the side of the detector, due to shorter distance to DArT . For this reason, a lead belt of 140 cm total height and 10 cm width has been placed the cryostat and the polyethylene shielding as it shown in Fig. 17.

B.   Background

The region of interest (ROI) is given by the ^{39}Ar β spectrum, with energy deposits in DArT between 0-600 keV.

The background events are going to deposit energy in DArT , ArDM or both. The energy deposited in ArDM is used to tag background events, considering 10 keV threshold. Therefore, the ultimate background are the events with an deposit energy in DArT in the ROI but *untagged* by ArDM.

Electronics was designed to be linear up to 1 MeV for DArT thus the pulse shape discrimination technique can be used in the ROI and only electron recoils represent a background for DArT.

For this reason, the background sources in DArT are:

- external γ fluxes coming from the surrounding rock in the hall were the detector is placed. The flux of γ's has been measured by the ArDM collaboration [6].

- γ's emitted by the different radio-impurities in materials of ArDM and DArT . The radioactivity levels for the different materials in ArDM was measured with high purity germanium detectors at LSC (except for the ArDM cryostat)
- β's from the plate-out of the ^{222}Rn daughters on the acrylic. ^{210}Bi contamination was assumed such as that measured in DEAP3600 after machining of a few diffusion lengths of Rn and then sanding in a Rn-reduced atmosphere.

For simplicity in the following we will call whatever is not external, internal background.
The values for the radio-impurities and mass of internal materials and the external background values are summarized in Tab. IV.

Source		^{238}U[mBq/kg]	^{232}Th[mBq/kg]	^{40}K[mBq/kg]	^{60}Co[mBq/kg]	^{210}Pb[Bq/kg]	^{210}Bi[mBq/m^2]	m[kg]	area[cm^2]
ArDMCryo		3.42	6.37	1.3	11.21			1630	
ArDM PMT's	Base	9176	11043	1978					
	Metal	181	73	371				10.8	
	Glass	636	115	53	2				
Lead Belt		0.37	0.073	0.31		10		6000	
ArDM pillars		0.012	0.04	0.06	0.04			16	
ArDM rings			3.42	6.37	1.3	11.21		2	
PMT's support		3.42	6.37	1.3	11.21			16	
Acrylic		0.004	0.005				0.22	1.8	514
DArTCu		0.012	0.04	0.06	0.04			6.95	
SiPM Arlon	Up	3.8							
	Mid	53	70	1300				0.001	
	Low	137							
Solder brazing		1203*	406*	3090*				0.001	
External		0.72**	0.13**	0.05**					406000

TABLE IV. Activities and masses for the different materials used for ArDM and DArTsimulation. The ^{238}U secular equilibrium in Arlon is broken. For this reason the upper, middle and lower part of the chain are considered. (*) Assumed value, it is necessary to look for a reference. (**) Flux of γ's per cm^2 .

The external background events are produced uniformly distributed. However, most of the external event that reach DArT come from the sides of the detector, due to the smaller distance that external γ's have to travel. For this reason, a lead belt was implemented around ArDM(Sec. VII A). The expected total background per week is shown Tab. IV.
The DArT active region is defined by the inner acrylic cylinder of volume 1019 cm^3 (equivalent to 1.42 kg of liquid argon). The number of signal events expected depends on the assumed ^{39}Ar depletion factor. Therefore, considering a depletion factor of 10 (with respect to atmospheric argon) after one pass of AAr through ARIA, the number of expected signal events is around 72.000. This corresponds to a signal to background ratio of 7 in the first configuration without the lead belt.
However, assuming larger depletion factors, e.g. the UAr with a radioactivity of 0.73 mBq/kg (631 events per week), the signal to background ratio is too small (≈ 0.06) to perform a meaningful measurement.
The second configuration including the lead belt allows to reduce the external background by a factor 65, and this would correspond to a signal to background ratio of 1.3 for the UAr.

Source	Evts/week in ROI	Evts untagged/week in ROI
ArDM Cryostat	3164.4	218.3
ArDM PMT's	1053.0	42.8
ArDM support pillars	0.4	0.2
ArDM support rings	14.0	0.3
ArDM PMT support	14.1	0.1
Lead Belt	150.5	16.2
DArT vessel	16.6	5.4
Arlon SiPM	40.9	23.5
Acrylic	5.3	2.7
Acrylic surface ^{210}Bi	3.7	3.7
Acrylic surface ^{210}Po	0.1	0.1
Solder brazing	4.2	0.3
External without the lead belt	117623.0	10020.5
Total without the lead belt	122098.9	10301.7
External with the lead belt	2596.2	155.7
Total with the lead belt	7209.9	465.5

TABLE V. Number of background events per week in ROI before and after the veto tagging due to the different materials. For the external background, configurations both with and without the lead belt are considered.

Another important feature is the shape of the background spectrum. The energy deposited in DArT per week is shown in Fig. 18 with a stacking of the material and external background events. Two different spectra are shown, before and after including the lead belt. In the first case (left), the external background (blue) dominates by far. In the second case, the external background is reduced and becomes of comparable size to the internal one.
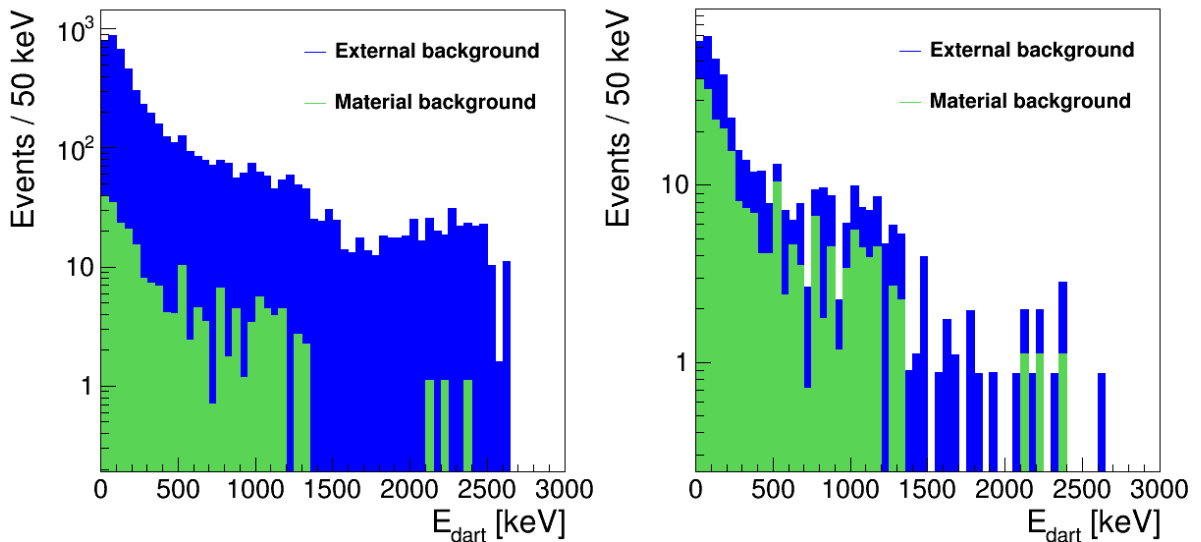

FIG. 18. Internal (green) and external (blue) γ background spectrum in DArT expected per week assuming a veto threshold of 10 keV. The spectra before (left) and after (right) including the lead belt shielding are shown.

The energy deposited in ArDM per week is shown in Fig. 19 with a stacking of the material and external background events. Two different spectra are shown, before and after including the lead belt. Different

peaks are clearly visible at 1450 keV, 1700 keV and 2600 keV, compatibles with γ 's coming from ^{40}K, ^{210}Bi and ^{206}Tl respectively.
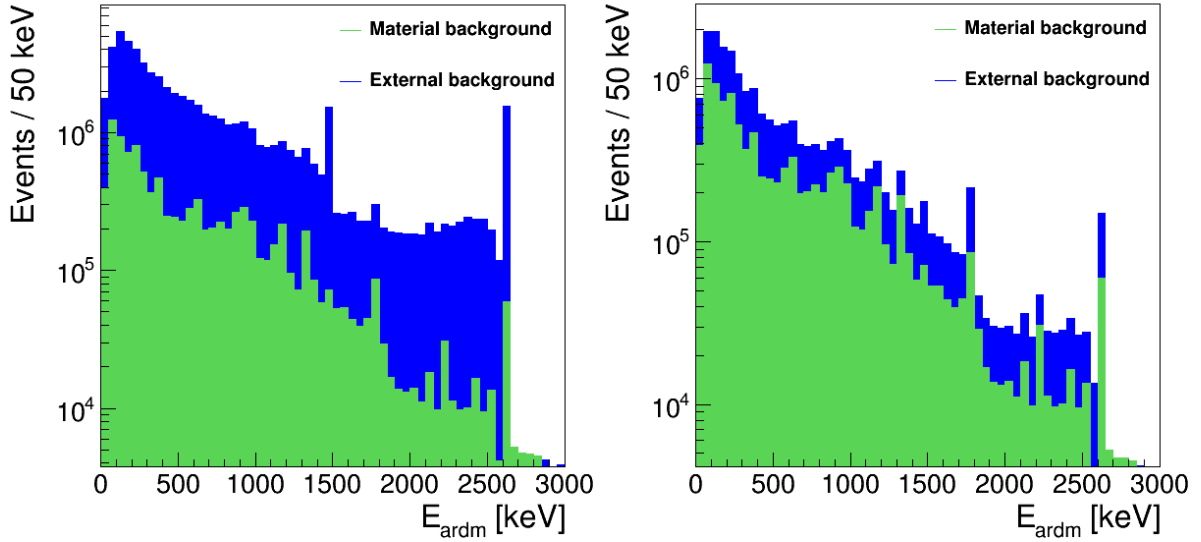

FIG. 19. Internal (green) and external (blue) γ background spectrum in ArDM expected per week. The spectra before (left) and after (right) including the lead belt shielding are shown.

Another possible source of background are the events coming from inner acrylic surface, due to ^{222}Rn daughter plate-out β events from ^{210}Bi and degraded α events after the interaction with the deposited TPB. The energy spectrum in DArT of surface ^{210}Bi and ^{210}Po events is shown in Fig. 20. There are events in the DArT ROI for both cases, although α events could be partially removed with pulse shape discrimination. For this reason, it is fundamental to have DEAP-style radon progeny control (0.22 mBq/m^2) for the DArT inner acrylic cylinder, this will reduce the number surface background to < 4 events untagged per week.
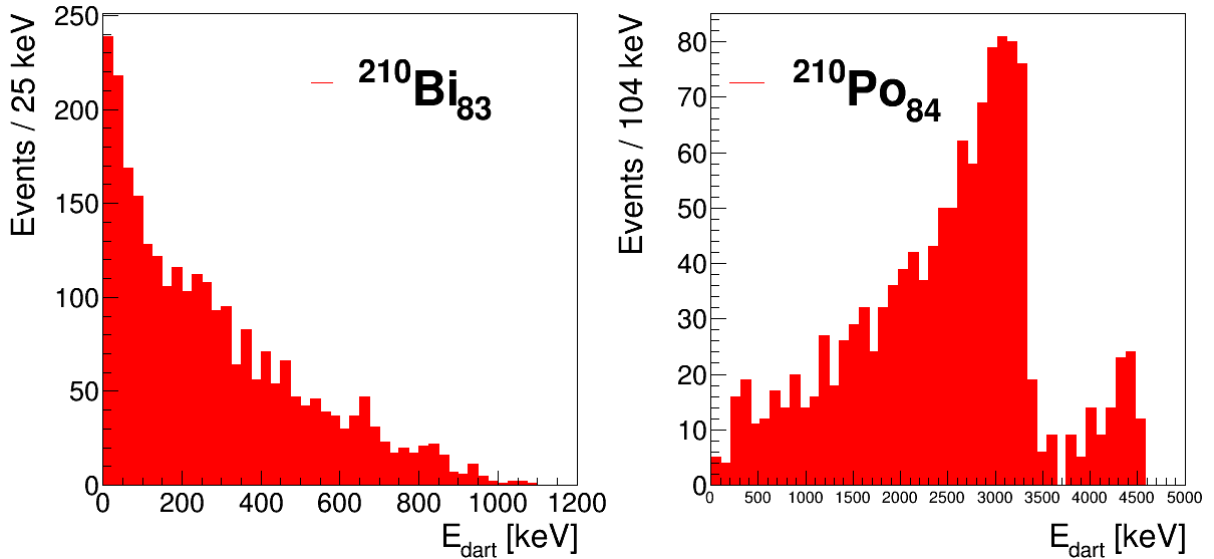

FIG. 20. ^{210}Bi surface β background spectra (left) and ^{210}Po surface α background spectra.

The current ArDM double phase geometry is able to detect events up to 10 keV using 24 PMT's. However, with only 11 PMT's and DArT shading some of the light, it is likely that the detection threshold will be in

fact larger, probably between a factor 2 and 3. The total number of background events in DArT is calculated as function of the veto energy threshold in the Fig. 21. The variation is linear with a slope of 8.5% every 10 keV.
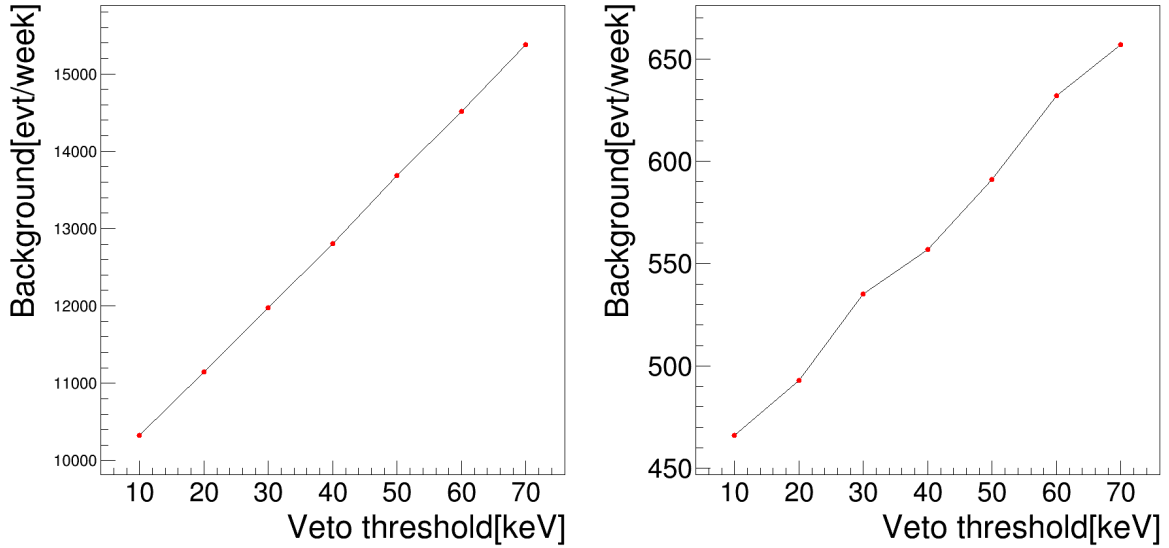

FIG. 21. Number of background events as a function of the veto threshold without the lead belt (left) and with the lead belt (right). The background increase is 8.5% every 10 keV.

C. Light response

The energy deposits in the liquid argon of DArT will produce photons that will be detected by the two SiPM at top and bottom sides of the active volume. The propagation of photons to the SiPMs, depends on a large number of optical properties of the detector materials and their interfaces. The relevant materials affecting the simulation are the liquid UAr, the acrylic (PMMA), the TPB coating of internal surfaces, the 3M foil reflector and the SiPMs planes.

The ultra-violet scintillation photons are converted by the TPB coating around the active volume to $\sim$ 420 nm. The visible photons cross the acrylic and they are reflected in the 3-M foil. At the end, the photons are collected by the SiPMs or lost in some dead area. Most of these materials are modelled as pure dielectrics, with the exceptions of the 3-M foil which is assumed metallic, i.e. a surface that photons cannot penetrate. All the internal PMMA surfaces are coated with a TPB. The TPB is assumed to re-emit a single visible (VIS) photon for each absorbed UV photon with a characteristic time of 1.5 ns.

The SiPMs are modelled as dielectric, but with an arbitrarily reduced absorption length, in order to fully absorb the transmitted visible photons in a few nanometers. Absorbed photons are converted to photo-electrons, with an efficiency of 0.4. All the remaining detector materials adopt standard GEANT4 modelling, with parameters tuned according to [11].

In order to evaluate the light response in the detector, 20,000 events of ^{39}Ar events have been simulated in the active volume. The mean energy for the ^{39}Ar β emission is 210 keV, thus considering a energy electron-ion pair production of 19.5 eV in liquid argon and a quenching factor of 0.95 for electrons, we expect around 10300 produced photons per event. The number of produced VUV-photons as coming from the simulation is 48.3/keV and are converted into visible photons with an efficiency of 0.985.

With reflector only on the detector sides, the average collection efficiency on the SiPMs turns out to be about 2.4%, that corresponds to a LY of 0.5 PE/keV, assuming 0.4 of photon detection efficiency (PDE). The light yield correspond to about 300 PE per SiPM for 1 MeV signal deposits. A possibility to increase the light yield is to add a reflector foil around the SiPM on both top and bottom caps, adding one special acrylic support to the previously described structure. The simulation shows that the LY can go up to 10 PE/keV. We keep this as an option in case after the first tests we verify the the LY is too low.

The average collection efficiency in the SiPM is represented in Fig. 22, as a function of the ^{39}Ar vertical

(left) and radial (right) interaction position in the argon. The top and bottom SiPM-planes are asymmetric respect to the Z position, when the event is closer to one the planes the collection efficiency is higher. The collection efficiency dependence with the radius interaction position is stronger for events close to the SiPMs for solid angle reasons. However, the total collection efficiency is uniform in the chamber. Therefore, the detector shows an adequate collection light efficiency. With reflector also on top and bottom caps a more uniform dependence vs radius was observed.
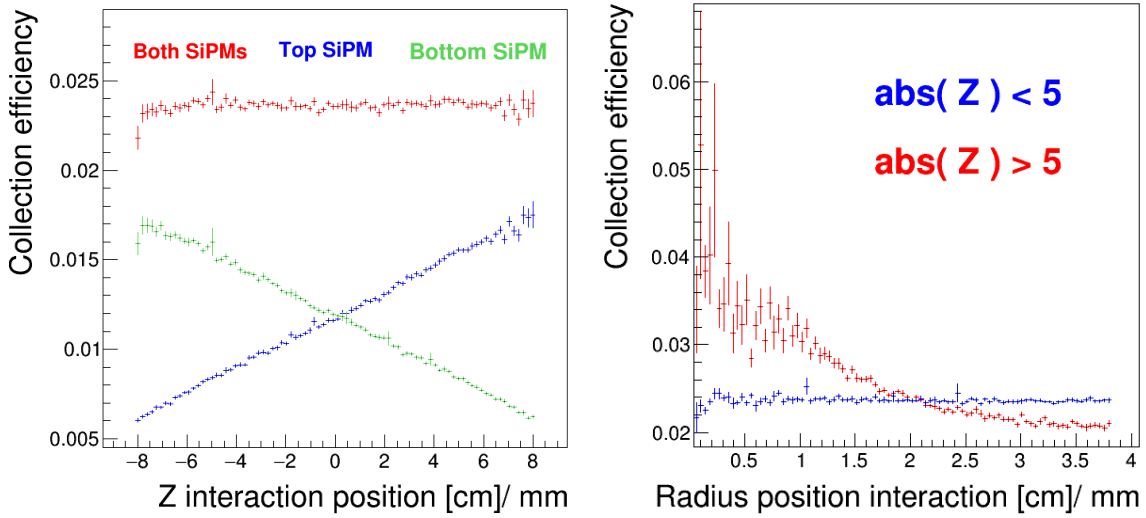

FIG. 22. Average collection efficiency vs height (left) and radius (right) of the interaction position in the detector. In this simulation there is no reflector on top and bottom cap and therefore for events closer to the SiPMs planes the collection efficiency dependence with the radius is stronger.

With reflector on both top and bottom plate, light collection efficiency turned out to be very sensitive to absorption coefficient of the acrylic. With the G4DS default value of $1.4\,\mathrm{m}$ at $420\,\mathrm{nm}$ the collection efficiency turned out to be 17.3% when the reflector was set also on top and bottom window. With the absorption coefficient corresponding the acrylic that we are going to implement in DArT the collection efficiency becomes 52%. Without the reflector on top and bottom plates the sensitivity to the acrylic absorption coefficient is less.

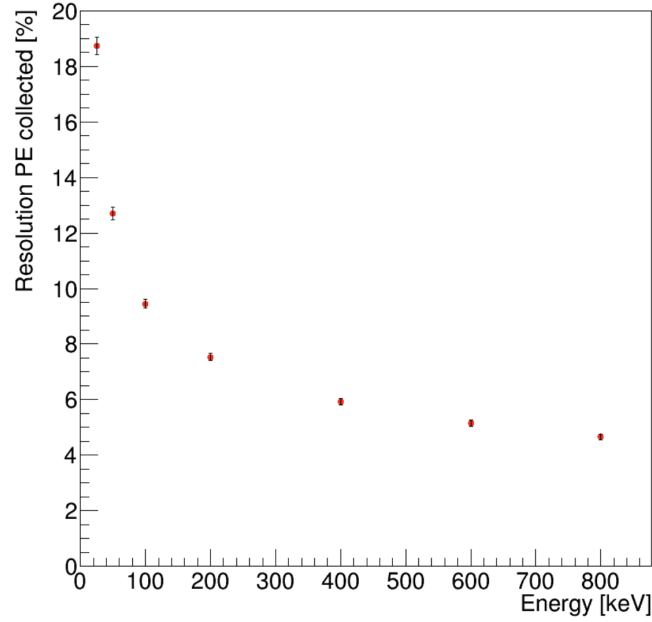The energy resolution of DArT is shown in Fig. 23.

FIG. 23. Energy resolution in DArT vs energy.

The optical simulation for the background events is too time consuming. For this reason, a look-up table has been developed based in the ^{39}Ar optical simulation.

The look-up table use the collection efficiency over the SiPM channels for the different energy deposit positions in the detector, using a grid of 1x1x1 cm cubes. The table is generated with 20000 events of ^{39}Ar using Gaussian distributions for the value in each cube. The number of generated photons from each energy deposits are calculated with Gaussian distributions considering the electron-ion pair production energy (19.5 eV) and the quenching factor. Finally a the number of photo-electrons was calculated assuming a Gaussian function of mean 0.4 and sigma 0.025.

D. Sensitivity

After the characterization of the background and the light response in DArT, it is possible to evaluate the sensitivity expected for the different argon depletions. In the following we calculate both the measurement uncertainty on the depletions in case a clear signal is observed and the 90% C.L upper limits in absence of an excess over the expected background.

A typical PE spectrum acquired with one week of running of DArT, with ^{39}Ar depletion factor of 10 respect to the AAr, is shown with black dots in Fig. 24. The total background is shown in red and ^{39}Ar signal is in blue. The total distribution is a randomized distribution generated from the sum of signal and background distributions. The ^{39}Ar content is extracted with a fit of the observed shape to the weighted sum of the red and blue histograms.
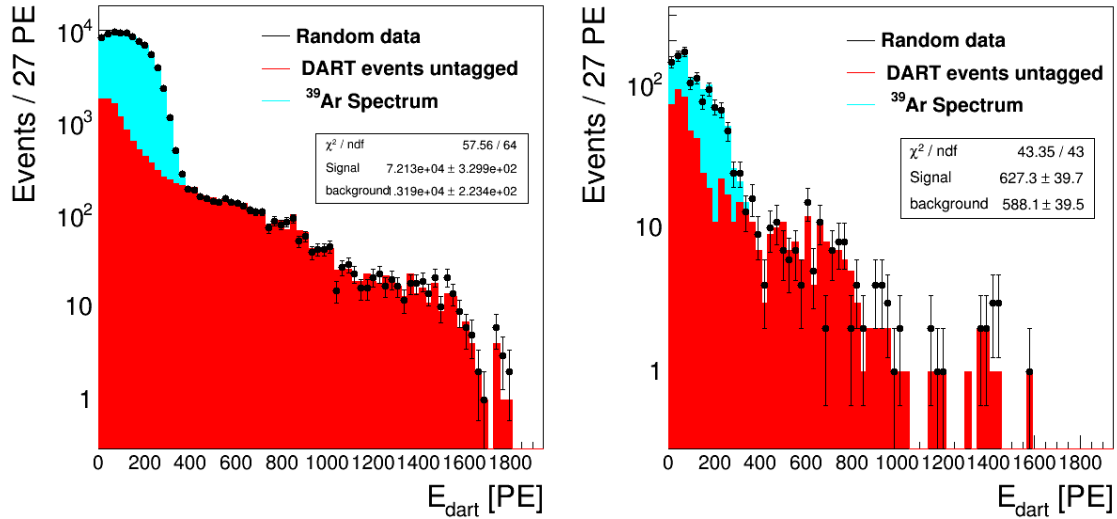
FIG. 24. Photo-electron spectrum corresponding to one week of data taking (black dots), with ^{39}Ar depletion factor of 10 without lead belt (left) and with ^{39}Ar depletions corresponding to the UAr with lead belt (right). The background spectrum is in red and ^{39}Ar signal is in blue.

Tab. VI shows the uncertainty that can be achieved on the measurement of the depletion factor per week with the different depletion factor of ^{39}Ar considering the configurations with and without the lead belt.

Depletion factor with respect to AAr	statistical uncertainty without lead [%]	statistical uncertainty with lead [%]
10	0.5	0.4
100	2.5	1.3
1400	20.3	6.7
14000	/	41.1

TABLE VI. Statistical uncertainty per week vs ^{39}Ar depletion factor with the two configurations without and with the lead belt.

The evaluation of the 90% C.L. upper limits to ^{39}Ar depletions was instead done only considering the number of events in the ROI as if they were in one energy bin and again neglecting systematics on the background knowledge. The complete calculation with the fit to the whole spectrum is underway.

90% C.L. upper limits on the depletions that can be measured are derived calculating the depletions that correspond in terms of number of events in the ROI to $1.64\,\sigma$ fluctuation of the background, assuming gaussian fluctuations. Only considering the statistical error on the background, from Tab. V these are 139 events without the lead belt and 35 events with the lead belt, corresponding to depletions of 6340 and 25200 respectively.

These preliminary results assume knowledge of the background shape from the Monte-Carlo and therefore do not include a systematic uncertainty.

In practice, however, the background shape in the ROI cannot be taken reliably from MC and will need to be derived from the data. The strategy that is going to be applied is to start from the total measured background spectrum (before using the tagging cut) and applying to it the veto cut efficiency vs E obtained from MC (which is most probably very well modelled and we assume to be correct to % precision).

A mixture of data and MC could be used to improve this estimate due to the different tagging efficiency for the various backgrounds as shown in Tab. V. We notice that the tagging rejection factors of the main internal backgrounds are around 14.5 for the cryostat and 24.6 for the PMT background. For the external they are

11.7 for the case without belt and 16.7 with the belt. For the case without the lead belt the background is totally dominated by the external one and so a correction factor on the total background shape can be a reliable estimate of the tagged background, to less than few % level. For the case with the lead belt cryostat background and external background are of similar size and also the PMT and internal background are sizable and we may expect larger uncertainty, probably at the 5% level or more. The study of these effect is underway. Also the ArDM energy spectra could be used in a global fit to improve the knowledge of the background spectrum.

The ^{39}Ar shapes can be obtained from the MC and validated with the AAr run and contribute to negligible systematic error.

E. Conclusions

In conclusion, the DArT sensitivity has been studied using the background and light response simulations. It shows a proper to design to operate with argon depletion factor up to 100 with the current ArDM design. The measurement of the UAr depletion factor requires a lead belt in order to reduce the external background. Systematic studies on the background shapes are underway.

VIII. ORGANIZATION AND TIME-TABLE

The *DArT in ArDM* project is supported by the whole DarkSide collaboration. Specific responsibilities and tasks of the Institutions for *DArT in ArDM* with an updated time-table are defined at the link https://docs.google.com/spreadsheets/d/1EYRkGFJ7dr8lEEmLc-oA0HHcF0y9HxLO8M9G-A682x4/edit?usp=sharing

IX. REQUESTS TO THE LSC

- approval to install the DArT chamber in ArDM
- approval to install the lead belt
- timely support in potential safety reviews that could be needed in this context
- continue to provide support for the infrastructure as done for ArDM
- the supply of lead for the lead belt and its support structure.

X. COST, PERSONNEL AND FUNDING

Many components of the DArT assembly come in-kind from the different participating institutions. Personnel will be provided by the participating institutions.

XI. TOWARDS A MEMORANDUM OF UNDERSTANDING

Given the high scientific relevance of the proposed experiment and its value for the experiments to come, a MOU between the proposing Collaboration and the LSC needs to be prepared and signed in due time.

The MOU will clarify formally the ownership of the *DArT in ArDM*, the collaboration and LSC duties and its exploitation rights for the years to come.

---

[1] P. Agnes et al. (The DarkSide Collaboration), Phys. Rev. Lett. **121**, 081307 (2018).
[2] P. Agnes et al. (The DarkSide Collaboration), Phys. Rev. Lett. **121**, 111303 (2018).
[3] P. Agnes et al. (The DarkSide Collaboration), Phys. Rev. D **98**, 102006 (2018).
[4] C. E. Aalseth et al. (The DarkSide Collaboration), Eur. Phys. J. Plus **133**, 131 (2018).

[5] J. Calvo et al., JCAP **1703**, 003 (2017).
[6] J. Calvo et al., JCAP **1812**, 011 (2018).
[7] P. A. Amaudruz et al., Astropart. Phys. **62**, 178 (2015).
[8] C. Jillings, AIP Conf. Proc. **1549**, 86 (2013).
[9] P. A. Amaudruz et al., Astropart. Phys. **108**, 1 (2019).
[10] P. A. Amaudruz et al., Phys. Rev. Lett. **121**, 071801 (2018).
[11] P. Agnes et al. (The DarkSide Collaboration), JINST **12**, P10015 (2017).